Research Square

Preprints are preliminary reports that have not undergone peer review.
They should not be considered conclusive, used to inform clinical practice,
or referenced by the media as validated information.

Effect of layer thickness on hot cracking in JBK-75 austenitic stainless steel fabricated by laser powder bed fusion

Wataru Mita
Nagaoka University of Technology
Magnus Neikter
University West
Sukhdeep Singh
The University of Osaka
Kota Kadoi
The University of Osaka
Tadachika Nakayama
nky15@vos.nagaokaut.ac.jp

Nagaoka University of Technology

Research Article

Keywords: Laser powder bed fusion, JBK-75, Hot cracking, Layer thickness, Grain boundary segregation, Scheil–Gulliver calculation

Posted Date: November 24th, 2026

DOI: https://doi.org/10.21203/rs.3.rs-11677293/v1

License: This work is licensed under a Creative Commons Attribution 4.0 International License.
Read Full License

Additional Declarations: No competing interests reported.

Effect of layer thickness on hot cracking in JBK-75 austenitic stainless steel fabricated by laser powder bed fusion

Abstract

JBK-75, a precipitation-hardened Fe–29Ni–14Cr austenitic stainless steel, is a candidate alloy for liquid-hydrogen rocket-engine components fabricated by laser powder bed fusion (PBF-LB); however, hot cracking hinders its application. In this study, cracks in JBK-75 built with layer thicknesses of 30 and 60 μm were quantified under ten combinations of laser power, scan speed and hatch distance, and the cracking mechanism was examined using scanning electron microscopy, electron backscattered diffraction (EBSD), electron probe microanalysis, and equilibrium and Scheil–Gulliver calculations with Thermo-Calc. The crack length density ranged from 1.06 to 2.34 mm/mm^2, and approximately 80% of the 442 measured cracks were hot cracks. Under identical scan parameters, the crack length density at 60 μm was 1.4–1.6 times that at 30 μm, mainly because the cracks were longer rather than more numerous. The crack length density decreased with increasing volumetric energy density E at 60 μm but showed no clear dependence at 30 μm; thus, E alone could not explain the layer-thickness effect. The crack examined by EBSD propagated along a high-angle grain boundary (HAGB); HAGBs accounted for 82.3% of all boundaries, and Ti and C, and weakly B, were enriched along the cracks. Thermodynamic calculations showed that TiC is the only phase crystallizing with the liquid, that Ti and B are enriched in the residual liquid, and that under Scheil conditions, 1% liquid persists to approximately 480 K below the equilibrium temperature. Cracking was minimized on the high-energy side, where porosity increases, indicating that densification and crack suppression require different process windows.

Keywords: Laser powder bed fusion, JBK-75, Hot cracking, Layer thickness, Grain boundary segregation, Scheil–Gulliver calculation

1. Introduction

JBK-75 is a precipitation-hardened austenitic stainless steel developed from the A-286 superalloy; it is an Fe–29Ni–14Cr alloy containing Ti, Mo and Al as the principal alloying additions [1–4]. Compared with A-286, its higher Ni content reduces the cracking susceptibility during casting and welding while maintaining strength [1,4]. The alloy exhibits excellent mechanical properties over a wide temperature range from −269 °C to 700 °C and a resistance to hydrogen embrittlement comparable to that of A-286 [5–7]. Owing to these properties, JBK-75 is being applied to components in which cryogenic liquid hydrogen and hot combustion gases come into contact within a single part, such as fuel injectors and cooling nozzles of liquid-hydrogen rocket engines, and it also forms the basis of HR-1, an alloy developed for additively manufactured rocket nozzles [1,7,8].

However, JBK-75 work hardens markedly and has poor machinability; consequently, machining greatly shortens tool life, and manufacturing complex components with internal channels requires considerable time and cost [9–12]. Near-net-shape fabrication by metal additive manufacturing (AM) has attracted attention as an effective solution to this problem [10,11,13]. Among metal AM processes, directed energy deposition (DED) offers high deposition rates but is limited in spatial resolution and surface quality [14], whereas laser powder bed fusion (PBF-LB) provides high dimensional accuracy and geometric freedom owing to its small beam diameter [13]. Furthermore, because the heat input in PBF-LB is highly localized, the cooling rates reach 10^4–10^6 K/s, producing a fine solidification microstructure [12,15,16]. This rapid cooling is also advantageous for suppressing the formation of the η phase (Ni_3Ti), which is problematic during aging [1,3].

Hot cracking in PBF-LB-built material, however, remains a major barrier to the practical application of this alloy system. Hot cracking is broadly classified into solidification cracking, which occurs when solidification shrinkage and thermal stress act on the liquid films remaining

at the final stage of solidification, and liquation cracking, which results from local melting of grain boundaries during reheating [17,18]. In alloys containing Ti, C and B, such as JBK-75, solidification segregation of these elements to grain boundaries is considered to promote the formation of low-melting liquid phases and thereby increase cracking susceptibility [18,19]. Similar cracking has been widely reported in Ni-based superalloys fabricated by PBF-LB, and its suppression remains a challenge [15,16,20].

Among the factors governing cracking, layer thickness directly alters the thermal history through the number of times the underlying layers are remelted by the melt pool, the cooling rate and the thermal stress. Layer thickness also determines the build time: doubling the layer thickness roughly halves the build time, so thicker layers are strongly desired from the viewpoint of productivity [3]. Using the same machine and design of experiments (DOE) as in the present study, Neikter et al. [3] built JBK-75 with layer thicknesses of 30 and 60 μm and reported porosities of 0.1% (30 μm) and 0.3% (60 μm, at a threefold build rate), increasing porosity at high energy density, an as-built tensile strength of 1110–1180 MPa with an elongation of approximately 20%, and Ti and C segregation at grain boundaries. Although cracks were observed, they were not quantified. Thus, the effect of layer thickness on crack density, whether cracking is also minimized under the conditions that minimize porosity, and the relationship between crack paths and segregation remain unclear.

This study therefore focused on hot cracking and aimed to answer three questions: (i) how much cracking occurs and how it changes with layer thickness; (ii) whether cracking can be predicted from the volumetric energy density alone; and (iii) where and why cracks form. Questions (i) and (ii) were addressed by quantifying the crack length and number densities at both layer thicknesses, and question (iii) by combining scanning electron microscopy (SEM), electron backscattered diffraction (EBSD) and electron probe microanalysis (EPMA) with equilibrium and Scheil–Gulliver calculations using Thermo-Calc.

2. Materials and methods

2.1. Powder and fabrication

Gas-atomized JBK-75 powder (Sandvik AB) was used as feedstock. The D10, D50 and D90 values of the particle size distribution were 19.7 ± 0.5, 33.9 ± 0.4 and 55.9 ± 0.2 µm, respectively, and the chemical composition is listed in Table 1. Specimens were built using an SLM 125 system (Nikon SLM Solutions AG) under an argon atmosphere with a laser spot diameter of 65 µm. Cubic specimens measuring 10 mm × 10 mm × 10 mm were built on a SUS316L build plate (Fig. 1). The build and DOE matrix were identical to those reported by Neikter et al. [3] and comprised 18 conditions in total, in which the laser power P, scan speed v and hatch distance h were varied for layer thicknesses t of 30 and 60 µm.

Table 1. Chemical composition of the JBK-75 powder (wt%).

Element	Fe	Ni	Cr	Ti	Mo	V	Al	C	B
JBK-75	Bal.	29.03	13.99	2.00	1.19	0.28	0.20	0.03	0.0014

In this study, five conditions per layer thickness—the four corners (L/L, H/L, L/H and H/H) and the center (M/M) of the P–v design—were analyzed, giving ten conditions in total (Table 2). Here, L, M and H denote the relatively low, medium and high levels within each layer thickness; the first letter refers to the level of P and the second to that of v. P was 150/200/250 W for t = 30 µm and 250/300/350 W for t = 60 µm, whereas v = 600/750/900 mm/s was common to both layer thicknesses. Note that, in the ten analyzed conditions, h varied together with v (0.10/0.12/0.14 mm); therefore, the effects of v and h cannot be separated. The volumetric energy density E was calculated as

$$E = \frac{P}{v \cdot h \cdot t} \tag{1}$$

where E is in J/mm^3, P in W, v in mm/s, and h and t in mm.

Table 2. Process parameters of the ten analyzed conditions.

Layer thickness t [μm]	Level (P/v)	P [W]	v [mm/s]	h [mm]	E [J/mm^3]
30	L/H	150	900	0.14	39.7
30	H/H	250	900	0.14	66.1
30	M/M	200	750	0.12	74.1
30	L/L	150	600	0.10	83.3
30	H/L	250	600	0.10	138.9
60	L/H	250	900	0.14	33.1
60	H/H	350	900	0.14	46.3
60	M/M	300	750	0.12	55.6
60	L/L	250	600	0.10	69.4
60	H/L	350	600	0.10	97.2

Conditions 30-H/L and 30-H/H have the same P, v and h (P = 250 W) as 60-L/L and 60-L/H, respectively, and differ only in layer thickness.

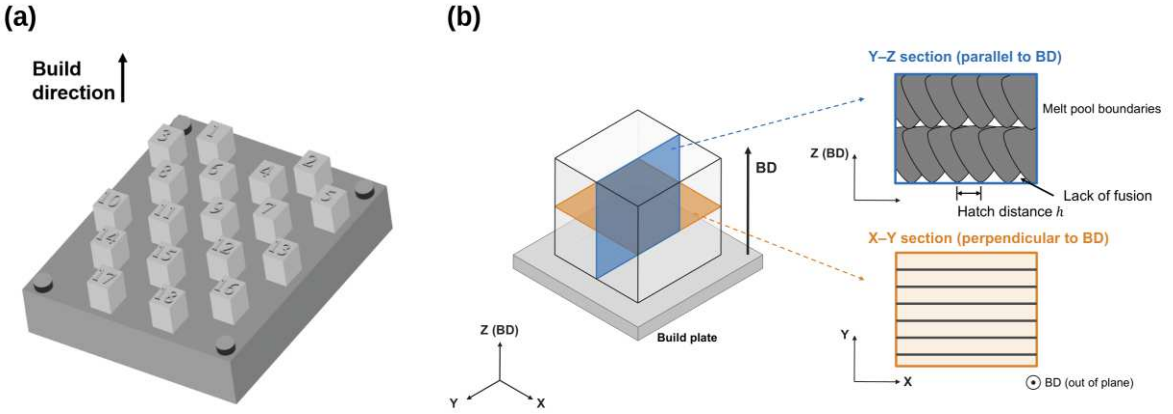


Fig. 1. (a) 10 mm cubic specimens on the SUS316L build plate and (b) schematic of the observed cross-sections (Y–Z section: parallel to the building direction; X–Y section: perpendicular to the building direction).

2.2. Sample preparation and microstructural observation

Y–Z cross-sections parallel to the building direction (BD) and X–Y cross-sections perpendicular to the BD were cut from each specimen (Fig. 1) and mounted in Bakelite resin. After grinding with SiC papers (#800–#2000) and polishing with diamond suspensions (6, 3 and 1 μm) to a mirror finish, the specimens were electrolytically etched in a 10 wt% aqueous oxalic acid solution at 2.5 V for 50 s. The specimens were observed using a scanning electron microscope (SEM: JIB-4700F, JEOL).

2.3. Crack quantification and classification

Following Ghoussoub et al. [21], cracking was quantified using two metrics: the crack length

density (mm/mm^2) and the crack number density (mm^{-2}). A 1 mm^2 region near the center of each cross-section was divided into fields of view, which were imaged and labeled A1, A2, …, A10 from left to right, with the row one field below labeled B1, B2, …. The magnification was fixed at ×500, and each field covered 0.04506 mm^2 (1280 × 880 pixels at 0.2 μm/pixel). Automatic extraction by thresholding deviated substantially from visual inspection; for example, a single crack was detected as several disconnected regions. Therefore, the cracks were measured manually in this study by tracing each crack as a polyline on the SEM images. Cracks lying intermittently along the same boundary were counted as a single crack, and equiaxed pores were excluded. The crack length was defined as the total length of the traced polyline. The crack length density L_A and crack number density N_A were calculated as

$$L_A = \frac{\sum_{i=1}^{N} l_i}{A}, \qquad N_A = \frac{N}{A} \tag{2}$$

where l_i is the length of the i-th crack, N is the number of cracks and A is the observed area. The mean crack length l_m was obtained as

$$l_m = \frac{L_A}{N_A} \tag{3}$$

Up to 20 fields (≤ 0.90 mm^2) were evaluated per condition; the number of fields analyzed for each condition is listed in Table 3. To avoid bias, each crack was classified on the basis of its morphology as a hot crack, a crack originating from a lack-of-fusion defect, a crack originating from a pore, or undetermined. Furthermore, the variance-to-mean ratio (VMR) of the number of cracks per field was calculated, and the spatial clustering of cracks was evaluated by a one-sided χ^2 test of the index of dispersion:

$$\mathrm{VMR} = \frac{s^2}{\mu}, \qquad \chi^2 = (m - 1) \cdot \mathrm{VMR} \tag{4}$$

where μ and s^2 are the mean and variance of the number of cracks per field, respectively, and m is the number of fields. For a random (Poisson) distribution, χ^2 follows a χ^2 distribution with $m - 1$ degrees of freedom.

2.4. EBSD

EBSD was performed to evaluate the crystal orientation and grain boundary character. After mechanical polishing, the surface deformation layer was removed by vibratory polishing, and the specimens were electrolytically etched under the same conditions as described in Section 2.2. Measurements were performed using an SEM (JIB-4700F, JEOL) equipped with a Symmetry detector (Oxford Instruments) at a step size of 0.085 μm, and the data were post-processed using AZtecCrystal. Inverse pole figure (IPF) maps were used to visualize grain morphology and orientation [22], and kernel average misorientation (KAM) maps were constructed to evaluate local misorientation, which is commonly used as a qualitative indicator of local plastic strain [23–25]. For grain boundary analysis, boundaries with misorientations below 5° were not counted as grain boundaries; boundaries with misorientations of $5° \leq \theta < 15°$ were defined as low-angle grain boundaries (LAGBs), and those of 15° or more as high-angle grain boundaries (HAGBs) [22]. This 5° threshold was applied only to boundary identification and not to the KAM calculation. KAM was calculated using a 3 × 3 kernel (first nearest neighbours), and misorientations exceeding 5° were excluded from the KAM calculation.

2.5. EPMA

Elemental segregation was evaluated using a wavelength-dispersive electron probe microanalyzer (EPMA: JXA-8530F, JEOL) at an accelerating voltage of 15 kV, a probe current of 0.1 μA, 500 × 500 points per map and a dwell time of 10 ms per point.

2.6. Thermodynamic calculations

Equilibrium and Scheil–Gulliver calculations were performed using Thermo-Calc 2023a (Thermo-Calc Software AB, Stockholm, Sweden) with the TCFE11 database [26,27]. The calculations were based on the powder composition listed in Ta ble 1 (Fe–29.0Ni–14.0Cr–2.0Ti–1.19Mo–0.28V–0.20Al–0.03C–0.0014B, wt%). In the equilibrium calculations, the temperature was varied from 300 to 1500 °C, and LIQUID, FCC_L12, FCC_A1,

NI3TI_D024, SIGMA, M6C and M23C6 were considered, with miscibility gaps enabled for FCC_L12 and FCC_A1. Because TCFE11 treats the MC carbide (TiC) and γ′ as additional composition sets of the FCC phase, FCC_L12#2, #3 and #1 in the results were assigned to the γ matrix, MC and γ′, respectively; NI3TI_D024 to the η phase; and M23C6_D84#1 and #2 to the boride ($M_{23}B_6$ type) and the $M_{23}C_6$ carbide, respectively. In the Scheil calculations, only LIQUID, FCC_L12 and FCC_A1 (γ and MC) were considered, and C and B were treated as fast-diffusing elements in the solid [28]. The Scheil calculations were terminated when the liquid fraction reached 1%. The partition coefficient k of each element was determined from the equilibrium calculation just below the liquidus (1390 °C) as

$$k = \frac{x_\gamma}{x_L} \tag{5}$$

where x_γ and x_L are the mole fractions of the element in γ and in the liquid, respectively.

3. Results

3.1. As-built microstructure

Fig. 2 shows an SEM image of the Y–Z cross-section of a specimen built with t = 30 μm. Grain boundaries appear as bright, continuous, wavy lines, and the grain interiors exhibit a cellular structure approximately 1 μm in size, which is characteristic of rapid solidification. In regions sectioned perpendicular to the growth direction, the cells appear as a honeycomb pattern, whereas in regions sectioned nearly parallel to the growth direction, they appear as elongated cells. The bright contrast of the cell boundaries indicates that solutes are enriched at the cell boundaries owing to solidification segregation. Both grain boundaries and cell boundaries are therefore potential crack paths.

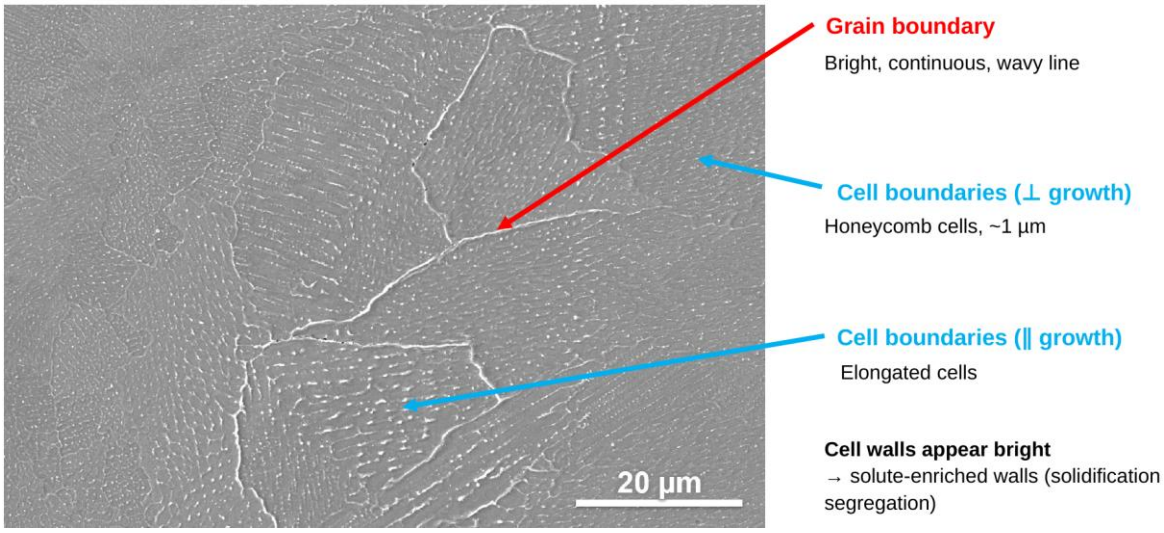


Fig. 2. SEM image of as-built JBK-75 (Y–Z cross-section, t = 30 µm). The grain boundary (red arrow) and cell boundaries (blue arrows) sectioned perpendicular (honeycomb cells) and parallel (elongated cells) to the growth direction are indicated.

3.2. Crack morphology and classification

Fig. 3 shows SEM images of representative cracks. The cracks were microcracks with lengths ranging from one to several tens of micrometers, and cracks crossing the cellular structure were rarely observed. In cross-sections parallel to the BD, the cracks propagated straight along the boundaries of columnar grains, whereas in cross-sections perpendicular to the BD, they formed short, branched networks, and the crack tips were continuous with bright, solute-enriched boundaries. Because both grain boundaries and cell boundaries exhibit bright contrast owing to solute enrichment (Fig. 2), the two could not be distinguished from the SEM images alone. The cracks thus propagated along solute-enriched boundaries, which is consistent with the characteristics of hot cracking. The crystallographic character of the cracked boundaries was examined by EBSD (Section 3.4).

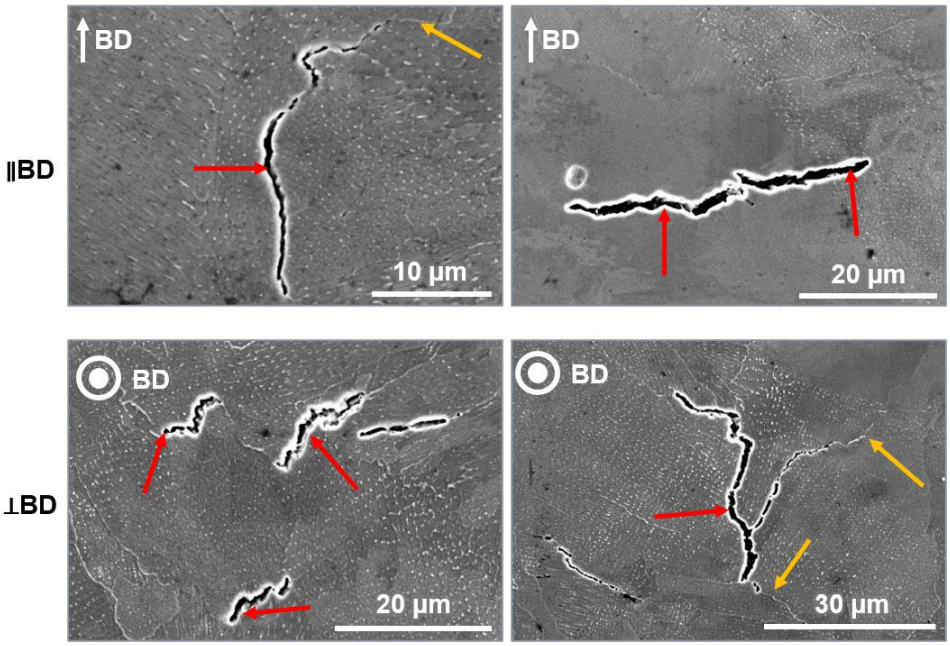


Fig. 3. SEM images of cracks. Top: parallel to the BD (∥BD); bottom: perpendicular to the BD (⊥BD). Red arrows indicate cracks, and yellow arrows indicate bright boundaries extending from the crack tips.

Of the 442 cracks measured under the ten conditions, 355 (80.3%) were hot cracks, 84 (19.0%) originated from defects and 3 (0.7%) were undetermined (Table 4). On a length basis, hot cracks accounted for 83.8%. The fraction of hot cracks ranged from 71% to 95% depending on the condition, and hot cracks constituted the majority under all conditions. The fraction of defect-originated cracks was 14.8% at 30 µm and 22.8% at 60 µm.

3.3. Process dependence on crack density

Fig. 4 shows the crack length density on *P*–*v* maps, and Table 3 summarizes the measurement results for each condition. The crack length density ranged from 1.06 to 2.34 mm/mm^2. The minimum was obtained under the H/L condition for both layer thicknesses (1.07 mm/mm^2 at 30 µm and 1.06 mm/mm^2 at 60 µm), and the maximum was obtained under M/M at 30 µm (1.62 mm/mm^2) and under L/H at 60 µm (2.34 mm/mm^2). The variation among conditions was small at 30 µm (1.07–1.62 mm/mm^2), whereas it exceeded a factor of two at 60 µm.

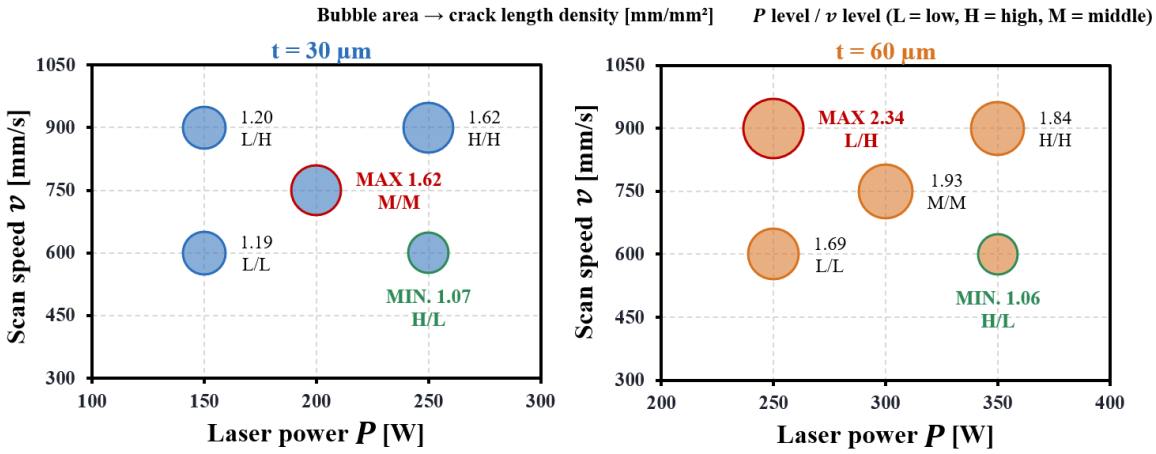


Fig. 4. Crack length density on *P*–*v* maps (bubble area ∝ crack length density). Left: *t* = 30 µm; right: *t* = 60 µm. Labels indicate the *P* level/*v* level.

Table 3. Crack measurement results for each condition.

t [µm]	Level	Fields	Area [mm²]	Cracks	Number density [mm⁻²]	Length density [mm/mm²]	Mean length [µm]	VMR
30	L/H	19	0.856	48	56.1	1.201	21.4	0.72
30	H/H	13	0.586	37	63.2	1.619	25.6	0.52
30	M/M	13	0.586	31	52.9	1.624	30.7	0.67
30	L/L	17	0.766	59	77.0	1.187	15.4	2.13*
30	H/L	14	0.631	35	55.5	1.072	19.3	0.54
60	L/H	12	0.541	46	85.1	2.342	27.5	1.18
60	H/H	20	0.901	60	66.6	1.842	27.7	1.61*
60	M/M	18	0.811	50	61.7	1.926	31.2	1.00
60	L/L	15	0.676	52	76.9	1.687	21.9	1.97*
60	H/L	14	0.631	24	38.0	1.057	27.8	0.67

* Significant spatial clustering of cracks according to the χ^2 test of the index of dispersion ($p < 0.05$; 30-L/L: $p = 0.005$; 60-H/H: $p = 0.044$; 60-L/L: $p = 0.016$).
Mean length = length density / number density (Eq. (3)).

The effect of layer thickness was examined by comparing the two pairs with identical *P*, *v* and *h* (*P* = 250 W). At *v* = 600 mm/s (30-H/L vs 60-L/L), the crack length density increased from 1.07 to 1.69 mm/mm², and at *v* = 900 mm/s (30-H/H vs 60-L/H), it increased from 1.62 to 2.34 mm/mm²; that is, in both cases, the value at 60 µm was 1.4–1.6 times that at 30 µm. The mean values for each layer thickness were 1.34 mm/mm² at 30 µm and 1.77 mm/mm² at 60 µm. At *v* = 600 mm/s, increasing *P* (L/L → H/L) decreased the crack length density for both layer thicknesses.

Fig. 5(a) shows the relationship between the crack length density and E. Because E at 60 µm is half that at 30 µm when P, v and h are identical, the two layer thicknesses were also compared at similar E. The 60 µm specimens with E = 33~46 J/mm^3 (1.84~2.34 mm/mm^2) exhibited higher crack length densities than the 30 µm specimen with E = 40 J/mm^3 (1.20 mm/mm^2); that is, even at comparable E, cracking was more severe at 60 µm. Hence, the data for the two layer thicknesses do not fall on a single curve against E. At 60 µm, the crack length density decreased almost monotonically with increasing E (Spearman's rank correlation coefficient, −0.9), whereas no clear dependence was observed at 30 µm. Fig. 5(b) shows the relationship between the crack number density and the mean crack length. Averaged over each layer thickness, the crack number density was nearly identical (60.9 mm^{-2} at 30 µm and 65.7 mm^{-2} at 60 µm), whereas the mean crack length increased from 22.5 to 27.2 µm. The higher crack length density at 60 µm therefore results mainly from longer cracks. As shown in Table 3, cracks were concentrated in particular fields for 30-L/L, 60-H/H and 60-L/L.

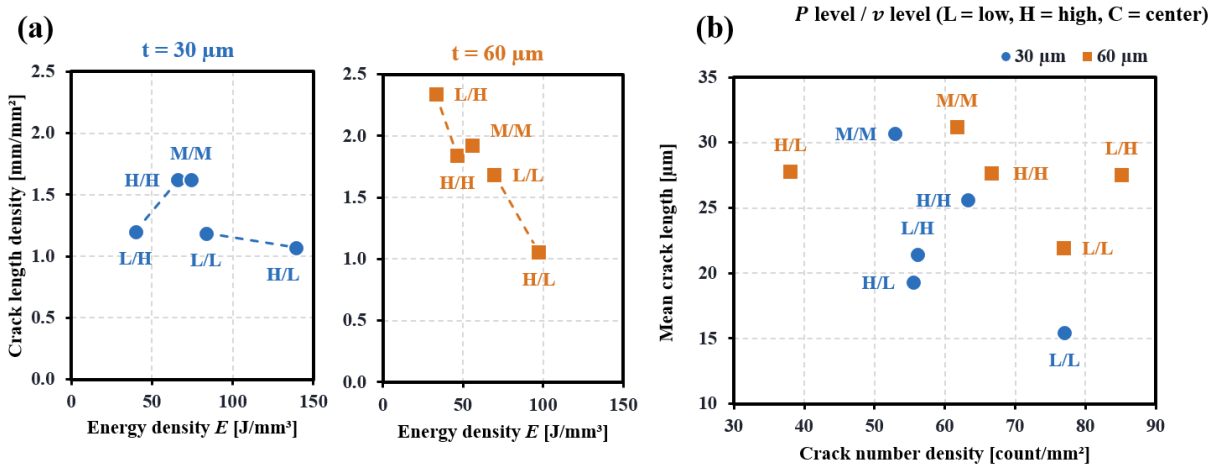


Fig. 5. (a) Crack length density versus volumetric energy density E (left: 30 µm; right: 60 µm). Dashed lines connect conditions with the same v (600 or 900 mm/s) and indicate the effect of P. (b) Mean crack length versus crack number density.

Table 4. Number of cracks by morphology.

t [µm]	Level	Total	Hot cracks	Defect-originated	Undetermined	Hot-crack fraction [%]
30	L/H	48	38	7	3	79
30	H/H	37	35	2	0	95

t [µm]	Level	Total	Hot cracks	Defect-originated	Undetermined	Hot-crack fraction [%]
30	M/M	31	29	2	0	94
30	L/L	59	47	12	0	80
30	H/L	35	27	8	0	77
60	L/H	46	36	10	0	78
60	H/H	60	47	13	0	78
60	M/M	50	42	8	0	84
60	L/L	52	37	15	0	71
60	H/L	24	17	7	0	71
Total		442	355	84	3	80

Defect-originated: cracks originating from lack-of-fusion defects or pores. Hot-crack fraction = hot cracks / total cracks.

3.4. Grain boundary character and elemental segregation at cracks

Fig. 6 shows EBSD and EPMA maps of the same crack. The microstructure consisted of columnar grains elongated along the BD, exhibiting epitaxial growth from the underlying layers [29]. The grains on either side of the crack showed markedly different orientations, and the crack coincided with a HAGB. This confirms that at least this crack propagated along a grain boundary rather than along cell boundaries within a grain. However, because only one crack was analyzed by EBSD, whether all cracks along the bright boundaries in Fig. 3 followed grain boundaries remains to be verified. KAM values increased along the crack, suggesting local strain concentration. Overall, HAGBs accounted for 82.3% of all boundaries and formed a connected network, consistent with reports that hot cracks in PBF-LB-built Ni-based alloys propagate along HAGBs [20].

Along the same crack, Ti and C signals were high, whereas Ni, Cr and Mo signals decreased inside the crack because of the absence of material. Al was locally enriched inside the crack; this is attributed to residual alumina abrasive particles trapped in the crack during polishing rather than to segregation. Ti was also enriched along uncracked grain boundaries, showing that Ti segregation was not limited to the crack. Weak B enrichment was also observed along the crack (arrows in Fig. 6), although the signal intensity was low because B is a light element present at only 0.0014 wt%.

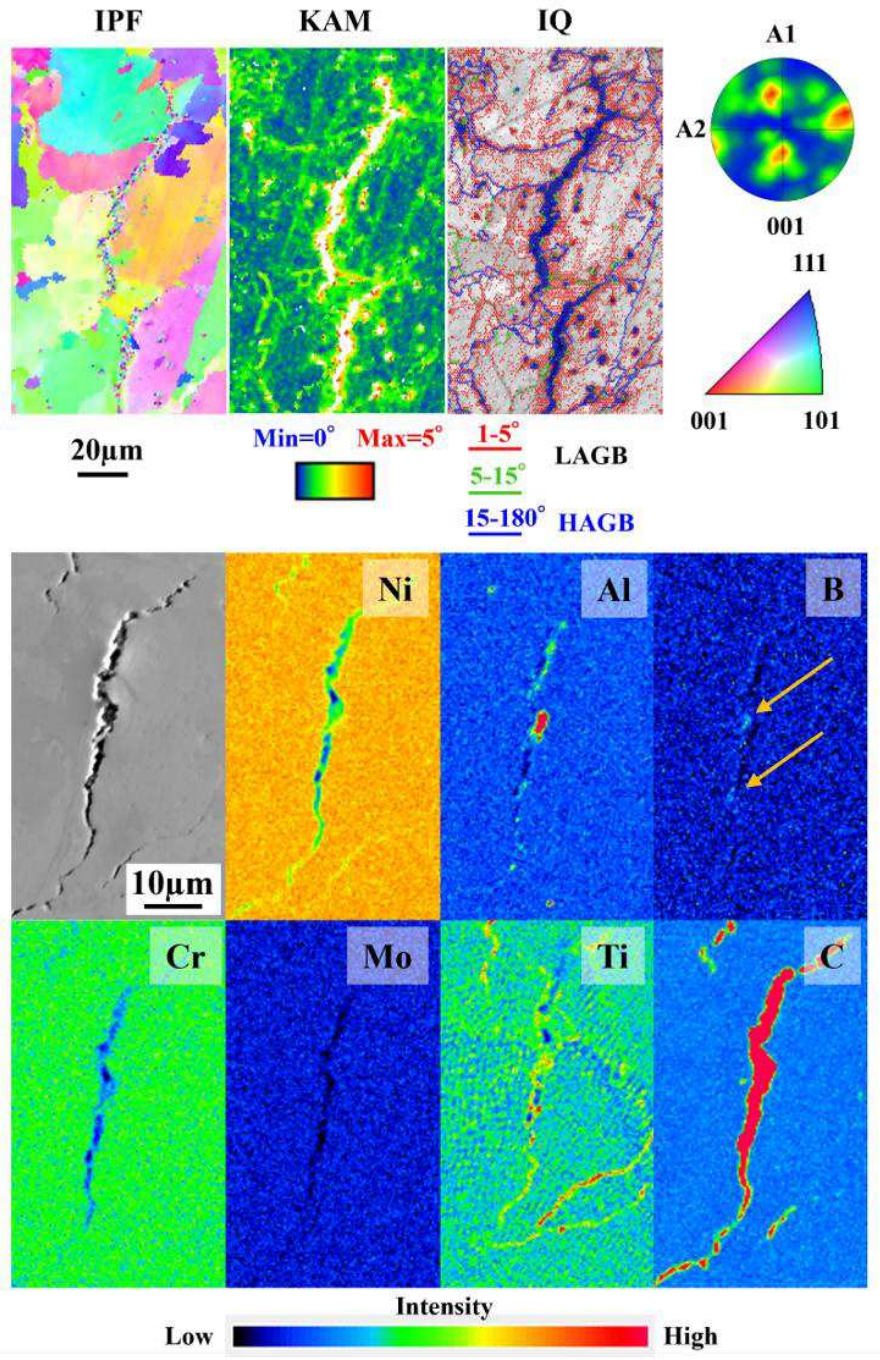


Fig. 6. EBSD (top) and EPMA (bottom) maps of the same crack (‖BD). Arrows in the B map indicate locations of weak B enrichment along the crack.

3.5. Thermodynamic calculations

Fig. 7 shows the phase fractions as a function of temperature obtained from the equilibrium calculation. On cooling, γ crystallized at 1395 °C and TiC (MC) at 1334 °C. TiC was the only phase that crystallized in coexistence with the liquid; the η phase (below 883 °C), σ phase

(below 647 °C), boride (below 613 °C), γ′ (below 504 °C) and $M_{23}C_6$ (below 428 °C) all formed in the solid state after the completion of solidification. The liquid fraction fell below 1% at 1300 °C, but the liquid did not disappear until 1190 °C. Because the η phase is the stable phase at equilibrium, γ′ appears only below 504 °C; during actual aging (approximately 720 °C), however, γ′ precipitates first as a metastable phase. Table 5 lists the partition coefficients just below the liquidus. Whereas *k* was close to unity for Fe, Cr and Ni, it was small for Ti (0.29), C (0.15) and B (0.005), indicating that these elements are rejected into the liquid during solidification.

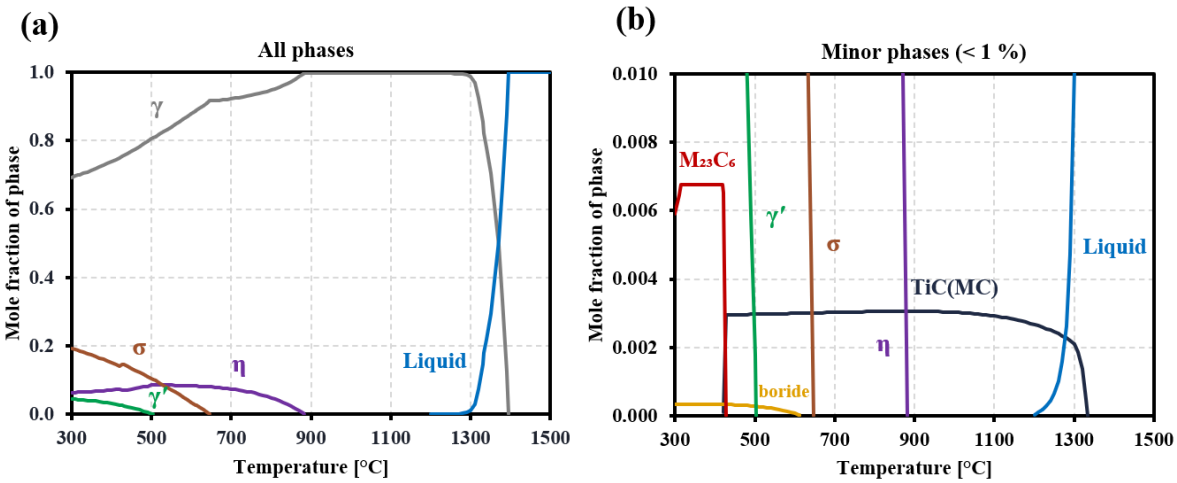


Fig. 7. Equilibrium phase fractions of JBK-75 as a function of temperature (Thermo-Calc 2023a, TCFE11): (a) all phases; (b) enlarged view of minor phases below 0.01.

Table 5. Partition coefficients $k = x_\gamma/x_L$ just below the liquidus (1390 °C).

Element	Fe	Cr	Ni	Mo	Ti	C	B
k	1.07	1.01	0.94	0.66	0.29	0.15	0.005

Fig. 8 shows the compositions of the liquid and the γ matrix calculated at equilibrium. With decreasing temperature, the mole fraction in the liquid increased from 0.023 to 0.13 (at 1190 °C) for Ti, from 0.0001 to 0.068 for B and from 0.28 to 0.34 for Ni, whereas those of Fe and Cr decreased. The C content of the liquid reached a maximum at 1334 °C, at which TiC begins to crystallize, and then decreased as C was incorporated into TiC. The Ti content of the γ matrix decreased below 880 °C owing to the formation of η and γ′.

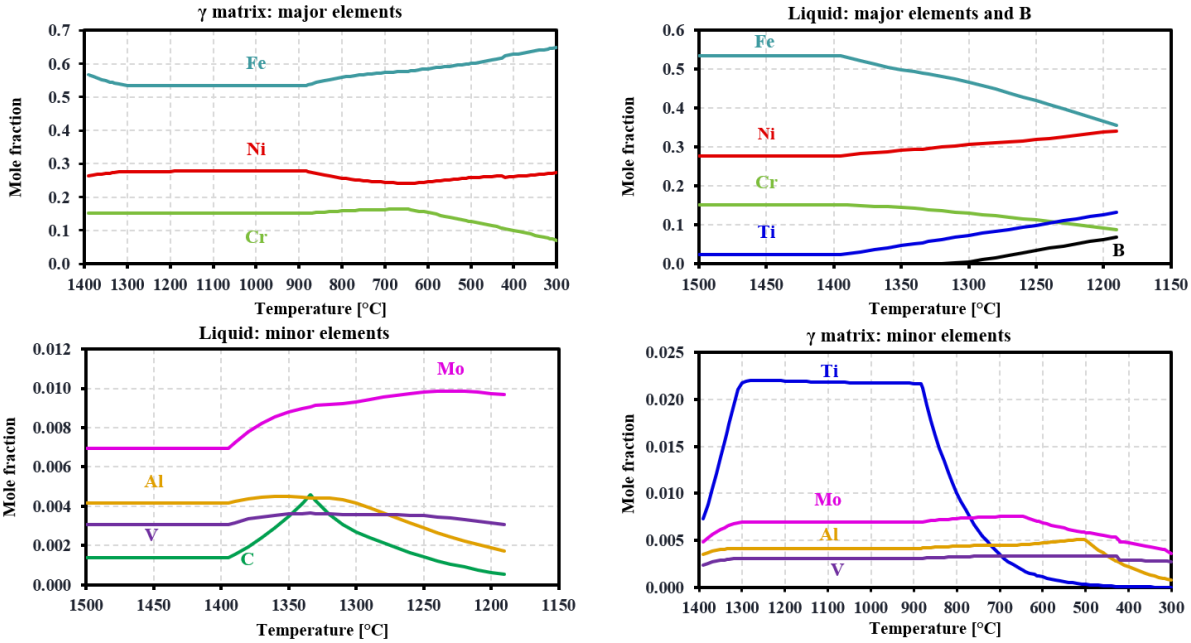
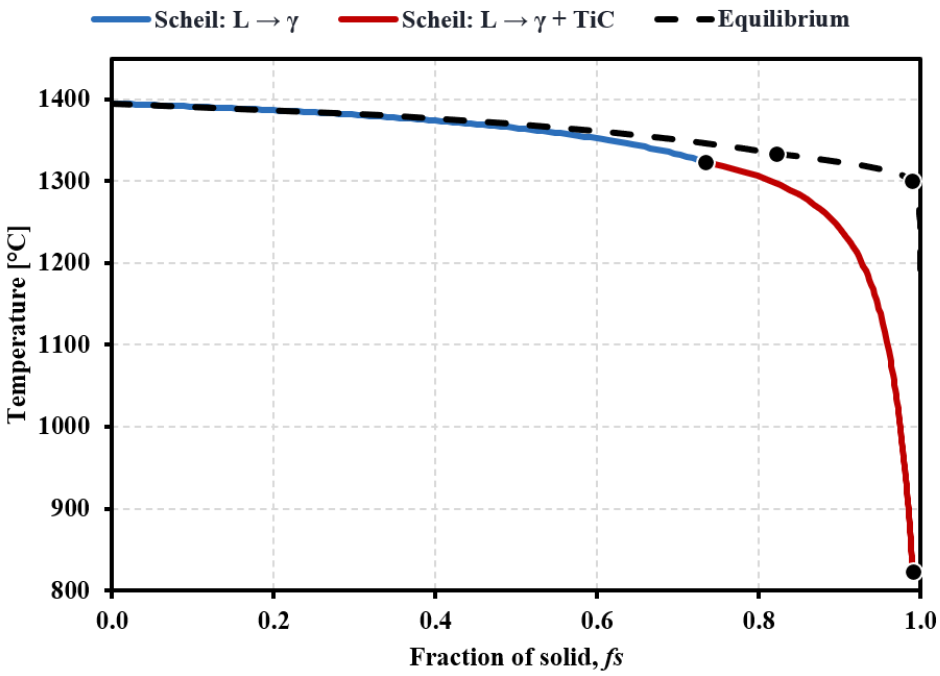


Fig. 8. Compositions of the liquid (1190–1500 °C, the range in which the liquid is stable) and the γ matrix obtained from the equilibrium calculation. Top: major elements and B, and minor elements in the liquid. Bottom: major and minor elements in the γ matrix.

Fig. 9 compares the solidification paths obtained from the Scheil and equilibrium calculations. The liquidus was 1395 °C in both cases, and TiC began to crystallize at a solid fraction of 0.73 (1324 °C) in the Scheil calculation and 0.82 (1334 °C) in the equilibrium calculation. The difference between the two became pronounced at the final stage of solidification: the temperature corresponding to a solid fraction of 0.99 was 1300 °C at equilibrium but 823 °C in the Scheil calculation. That is, under rapid-cooling conditions in which solid-state diffusion of the substitutional elements is negligible, the last 1% of the liquid persists to a temperature approximately 480 K lower than that at equilibrium.



306

307 **Fig. 9.** Comparison of the solidification paths obtained from the Scheil–Gulliver and equilibrium
308 calculations (Thermo-Calc, TCFE11). Because the Scheil calculation was terminated at a liquid fraction
309 of 1%, 823 °C is not the temperature at which the liquid disappears.

310 **4. Discussion**

311 ***4.1. Cause and mechanism of hot cracking***

312 The present results indicate that the cracks in PBF-LB-built JBK-75 are hot cracks that form
313 where three factors—a metallurgical cause, a mechanical driving force and a crack site—
314 overlap at grain boundaries (Fig. 10).

315 The cause is a low-melting liquid film resulting from solidification segregation. Ti, C and B,
316 which have small partition coefficients, are rejected into the liquid during solidification (Table
317 5); C is fixed as TiC below 1334 °C, whereas Ti and B continue to be enriched in the residual
318 liquid (Fig. 8). The enrichment of Ti and C along the cracks observed by EPMA (Fig. 6) is
319 consistent with the presence of a Ti-rich final liquid and TiC particles. The liquid film remaining
320 at the cracked grain boundaries is therefore interpreted as a Ti-rich liquid with C present as TiC,
321 rather than a liquid enriched in both Ti and C. The calculations indicate that B is also strongly
322 enriched and may contribute to lowering the melting point of the liquid film [30,31]. Consistent

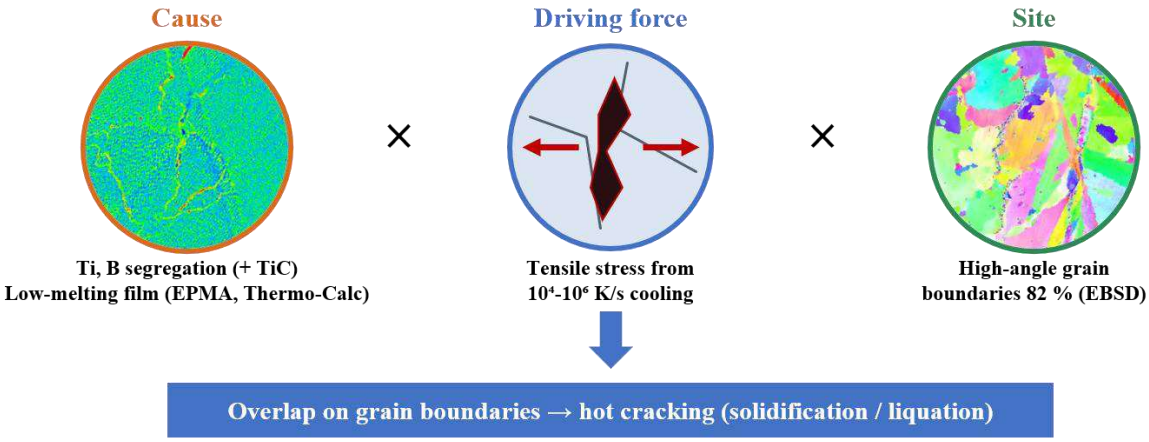
with this, weak B enrichment was observed along the crack by EPMA (Fig. 6). Because the solubility of B in γ is extremely low and the equilibrium calculation predicts the formation of a boride ($M_{23}B_6$ type; Fig. 7), the B detected along the crack may be present as borides rather than as free B. Borides are low-melting phases and may liquate during reheating by the deposition of subsequent layers, thereby also contributing to liquation cracking [32–34] Nevertheless, the presence of free B cannot be excluded; free B segregated to grain boundaries has been shown to lower the local liquation temperature and promote continuous liquid films in a cast Ni-based superalloy [31], and its distribution could be clarified by techniques with higher sensitivity to light elements, such as secondary ion mass spectrometry (SIMS) or atom probe tomography (APT). The driving force is the tensile strain associated with rapid cooling. Austenitic alloys such as JBK-75 have a large coefficient of thermal expansion, and the rapid cooling in PBF-LB generates high tensile residual stresses, and fully austenitic stainless steels have been shown to exhibit solidification cracking even under laser welding conditions [35]. Rapid cooling suppresses precipitates that require time for diffusion, such as the η phase, but it intensifies solidification segregation and widens the temperature range over which liquid films persist (Fig. 9). The thermal contraction strain imposed on the solid skeleton while the liquid films persist is proportional to the temperature drop:

$$\varepsilon_{\mathrm{th}} \approx \alpha \Delta T \tag{6}$$

where α is the coefficient of thermal expansion and ΔT is the temperature interval over which the liquid films persist. ΔT was evaluated over the solid-fraction range of 0.90–0.99 for both calculations. This range corresponds to the vulnerable stage of solidification, in which the solid forms a coherent network that transmits strain while liquid films remain between the grains and can no longer be replenished by liquid feeding [[36]]; the upper limit of 0.99 also coincides with the termination of the Scheil calculation at a liquid fraction of 1%. Assuming $\alpha \approx 17 \times 10^{-6}$ K^{-1}, ε_(th) over this range is approximately 0.03% at equilibrium (ΔT ≈ 20 K) and

approximately 0.7% under Scheil conditions ($\Delta T \approx 420$ K). Even if the equilibrium interval is extended to the complete disappearance of the liquid (solid fraction 0.99–1.00, $\Delta T \approx 110$ K), $\varepsilon_{(th)}$ is only approximately 0.2%, still much smaller than under Scheil conditions. Rapid cooling further increases the strain rate and hinders liquid feeding. This competition between the strain rate and liquid feeding in the mushy zone has been formalized in the criteria proposed by Kou [37] and by Rappaz et al. [38]. Rapid cooling is thus beneficial for suppressing the η phase but detrimental with respect to hot cracking.

The crack examined by EBSD was located at a HAGB. Because HAGBs have high grain boundary energy, they are readily wetted by liquid films, and the bridging of grains with large misorientations requires greater undercooling; consequently, liquid films tend to persist to lower temperatures at HAGBs, and cracking has been shown to occur preferentially at HAGBs in Ni-based superalloys [39–41]. In addition, the increase in KAM along the cracks (Fig. 6) suggests that strain is concentrated at these boundaries. The fact that HAGBs account for 82.3% of all boundaries owing to the epitaxially grown columnar grains and form a connected network is consistent with the frequent occurrence of cracks. However, the Ti and C enrichment detected by EPMA and the HAGBs are conditions common to both solidification and liquation cracking and therefore cannot distinguish between them. Moreover, because the classification in this study was based on SEM cross-sectional images, hot cracks were not subdivided into solidification and liquation cracks. In multilayer builds, reheating by the irradiation of subsequent layers can cause local melting of segregated grain boundaries through constitutional liquation [32,33]; thus, the observed hot cracks may include liquation cracks. The two types differ only in the origin of the liquid film—residual liquid at the end of solidification or remelting during reheating—and are considered to be continuous phenomena that share the same cause, driving force and site.



372

373 **Fig. 10.** Mechanism of hot cracking in PBF-LB-built JBK-75. Cracks form where three factors overlap
374 at grain boundaries: the cause (low-melting liquid film due to Ti and B segregation, possibly involving
375 borides; EPMA and thermodynamic calculations), the driving force (tensile stress due to rapid cooling
376 at 10^4–10^6 K/s) and the site (HAGBs accounting for 82% of all boundaries; EBSD).

377 ***4.2. Effect of layer thickness and volumetric energy density***

378 Although *E* is widely used as an index of heat input, in this study, cracking at 60 µm was more
379 severe than at 30 µm even at comparable *E*, and the data for the two layer thicknesses did not
380 fall on a single curve against *E* (Fig. 5(a)). This is presumably because *E* represents only the
381 heat input per unit volume and does not capture the thermal history, that is, how many times
382 each layer is remelted. Table 6 compares the two layer thicknesses. The remelting ratio D/t,
383 defined as the ratio of the melt pool depth D to the layer thickness t, is estimated to correspond
384 to three to four underlying layers at 30 µm and one to two at 60 µm. Here, D is measured from
385 the top surface of the current layer to the bottom of the melt pool. The hot-crack number density
386 was almost the same for the two layer thicknesses (51.6 mm^{-2} at 30 µm and 50.4 mm^{-2} at
387 60 µm); the effect of layer thickness appeared not in the number but in the length of the hot
388 cracks. In contrast, the number density of defect-originated cracks was higher at 60 µm
389 (8.7 mm^{-2} at 30 µm vs 15.2 mm^{-2} at 60 µm). The observation that the number of hot cracks is
390 independent of layer thickness whereas only their length differs may be explained by the healing
391 and segmentation of cracks through remelting. When a new melt pool remelts the underlying
392 layers, the portions of pre-existing cracks within the melt pool disappear, and the cracks are

truncated at the remelted depth. In thin layers, which are remelted more times, cracks are kept short, whereas in thick layers with shallow remelting, cracks are likely to survive and extend along columnar grain boundaries across multiple layers.

Table 6. Comparison between the two layer thicknesses (mean of five conditions for each layer thickness).

Item	30 µm	60 µm
Number of remelted underlying layers (D/t, schematic estimate)	3–4	1–2
Hot-crack number density [mm^{-2}]	51.6	50.4
Number density of defect-originated cracks [mm^{-2}]	8.7	15.2
Mean crack length [µm]	22.5	27.2
Dependence of crack length density on E	Almost constant (1.07–1.62)	Decreasing (2.34 → 1.06)

D/t is not a measured value and needs to be verified by measuring melt pool depths on etched cross-sections.

This hypothesis also explains the marked decrease in cracking with increasing E at 60 µm. As E increases, the melt pool deepens, D/t increases and the healing effect becomes stronger. This trend is opposite to that reported for alloy 718 in hot cracking tests simulating AM, in which the solidification cracking susceptibility increased with laser power owing to the change in penetration shape [16]; in multilayer builds, crack healing by remelting may outweigh such an increase. At 30 µm, by contrast, D/t is already large under all conditions, so the effect of E is considered to be small. The longer cracks at 60 µm (Fig. 5(b)) can likewise be interpreted as a result of less segmentation by remelting, which allows cracks to survive over long distances along columnar grain boundaries. However, because D/t was not measured in this study, these interpretations remain hypothetical. Future work should measure the melt pool depths on etched cross-sections, plot the crack density against D/t, and examine whether the data for both layer thicknesses collapse onto a single relationship.

4.3. Process windows for porosity and cracking

For both layer thicknesses, cracking was minimized under the H/L condition, which had the highest E within each layer thickness (138.9 J/mm^3 at 30 µm and 97.2 J/mm^3 at 60 µm). In

414 contrast, the porosity of the same set of specimens has been reported to increase on the high-
415 energy-density side [3], which is attributed to keyhole porosity, whereby deep, unstable melt
416 pools entrap vapor cavities [42,43]. On the low-energy-density side, lack-of-fusion defects form
417 owing to insufficient overlap between melt pools [44,45]. The minimum porosity was obtained
418 at 30 μm under an intermediate heat input (132 W, 750 mm/s) [3]. Thus, for this alloy, the
419 conditions that minimize porosity do not coincide with those that minimize cracking, and
420 densification and crack suppression require different process windows. This difference is
421 attributed to the fact that porosity is governed by the geometric stability of the melt pool,
422 whereas cracking is governed by the thermal history during solidification and grain boundary
423 segregation.

424 Complete suppression of cracking by optimizing the process parameters alone is likely to be
425 difficult. A combination of the following approaches is expected to be effective: disrupting the
426 HAGB network by grain refinement and the formation of equiaxed grains through inoculant
427 addition [46,47]; suppressing liquid film formation by controlling Ti, C, B and impurity
428 elements [30]; and relieving thermal stress through preheating and scan strategies [15,48].

429 **5. Conclusions**

430 Cracks in JBK-75 fabricated by PBF-LB with layer thicknesses of 30 and 60 μm were
431 quantified, and the cracking mechanism was investigated by microstructural analysis and
432 thermodynamic calculations. The main conclusions are as follows.

433 (1) The crack length density ranged from 1.06 to 2.34 mm/mm^2, and approximately 80% of the
434 observed cracks (84% on a length basis) were hot cracks along solute-enriched boundaries.
435 (2) Under identical P, v and h, the crack length density at 60 μm was 1.4–1.6 times that at 30 μm.
436 Cracking was also more severe at 60 μm when compared at similar E, and the higher crack
437 length density at 60 μm resulted mainly from longer cracks.
438 (3) At 60 μm, cracking decreased with increasing E, whereas no clear dependence was observed

at 30 μm; thus, E alone could not account for the effect of layer thickness.

(4) The crack examined by EBSD propagated along a HAGB; HAGBs accounted for 82.3% of all grain boundaries, and Ti and C were enriched along the cracks. Thermodynamic calculations showed that TiC is the only phase crystallizing with the liquid, that Ti and B are enriched in the residual liquid, and that under rapid cooling the last 1% of liquid persists to approximately 480 K below the equilibrium temperature. The cracks are attributed to the overlap of a low-melting liquid film due to Ti segregation, tensile stress due to rapid cooling, and HAGBs.

(5) For both layer thicknesses, the condition that minimized cracking lay on the high-energy side, where porosity increases, indicating that densification and crack suppression require different process windows. The hot-crack number density was nearly independent of layer thickness, and the effect of layer thickness appeared in the crack length. This may be explained by the healing and segmentation of cracks through remelting, and verification by measuring the remelting ratio D/t is a subject for future work.

Declarations

Competing interests: The authors declare that they have no known competing financial interests or personal relationships that could have appeared to influence the work reported in this paper.

Data availability

Data will be made available on request.

Funding: Details of funding are provided on the separate title page to preserve anonymity during double-blind review.

Author contributions: Provided on the separate title page.

References

[1] Z.C. Jones, P.R. Gradl, Powder Bed Fusion Additive Manufacturing of JBK-75, NASA

Marshall Space Flight Center, 2019.

[2] J.A. Schneider, G. Puerto, E. Walker, B.T. Montgomery, P.R. Gradl, B. Walker, M. Santangelo, S. Thompson, Wire Based Directed Energy Deposition of JBK-75, Metallurgical and Materials Transactions A 55 (2024) 1098–1110. https://doi.org/10.1007/s11661-024-07306-x.

[3] M. Neikter, P. Bhaskar, S. Singh, K. Kadoi, C. Lyphout, F. Svahn, R. Pederson, Tensile properties of laser powder bed fusion built JBK-75 austenitic stainless steel, Materials Science and Engineering: A 874 (2023) 144911. https://doi.org/10.1016/j.msea.2023.144911.

[4] R.L. Page, R.W. Krenzer, Summary of mechanical properties for JBK-75 forgings, Rockwell International, Rocky Flats Plant, 1979. https://doi.org/10.2172/6167407.

[5] A.W. Thompson, J.A. Brooks, Hydrogen performance of precipitation-strengthened stainless steels based on A-286, Metallurgical Transactions A 6 (1975) 1431–1442. https://doi.org/10.1007/BF02641935.

[6] C. San Marchi, B.P. Somerday, Technical reference for hydrogen compatibility of materials, Sandia National Laboratories, 2012. https://doi.org/10.2172/1055634.

[7] P.K. Liaw, W.A. Logsdon, M.H. Attaar, Automated Near-Threshold Fatigue Crack Growth Rate Testing of JBK-75 Stainless Steel at Cryogenic Temperatures, in: Austenitic Steels at Low Temperatures, Springer US, 1983: pp. 171–185. https://doi.org/10.1007/978-1-4613-3730-0_10.

[8] P.R. Gradl, Successes and Failures of Metal Additive Manufacturing for Rocket Engines, NASA (Technical Reports Server), 2023. https://ntrs.nasa.gov/citations/20210022989.

[9] A.P. McManigle, A.W. Simonis, JBK-75 stainless steel machinability study, Rockwell International, Rocky Flats Plant, 1993. https://doi.org/10.2172/10192352.

[10] M. Srivastava, S. Rathee, V. Patel, A. Kumar, P.G. Koppad, A review of various materials for additive manufacturing: Recent trends and processing issues, Journal of Materials Research and Technology 21 (2022) 2612–2641. https://doi.org/10.1016/j.jmrt.2022.10.015.

[11] B. Blakey-Milner, P. Gradl, G. Snedden, M. Brooks, J. Pitot, E. Lopez, M. Leary, F. Berto, A. du Plessis, Metal additive manufacturing in aerospace: A review, Materials & Design 209 (2021) 110008. https://doi.org/10.1016/j.matdes.2021.110008.

[12] T. DebRoy, H.L. Wei, J.S. Zuback, T. Mukherjee, J.W. Elmer, J.O. Milewski, A.M. Beese, A. Wilson-Heid, A. De, W. Zhang, Additive manufacturing of metallic components – Process, structure and properties, Progress in Materials Science 92 (2018) 112–224. https://doi.org/10.1016/j.pmatsci.2017.10.001.

[13] W.E. King, A.T. Anderson, R.M. Ferencz, N.E. Hodge, C. Kamath, S.A. Khairallah, A.M. Rubenchik, Laser powder bed fusion additive manufacturing of metals; physics, computational, and materials challenges, Applied Physics Reviews 2 (2015) 041304. https://doi.org/10.1063/1.4937809.

[14] D. Svetlizky, M. Das, B. Zheng, A.L. Vyatskikh, S. Bose, A. Bandyopadhyay, J.M. Schoenung, E.J. Lavernia, N. Eliaz, Directed energy deposition (DED) additive manufacturing: Physical characteristics, defects, challenges and applications, Materials Today 49 (2021) 271–295. https://doi.org/10.1016/j.mattod.2021.03.020.

[15] L.N. Carter, C. Martin, P.J. Withers, M.M. Attallah, The influence of the laser scan strategy on grain structure and cracking behaviour in SLM powder-bed fabricated nickel superalloy, Journal of Alloys and Compounds 615 (2014) 338–347. https://doi.org/10.1016/j.jallcom.2014.06.172.

[16] K. Kadoi, Y. Matsumoto, H. Chiba, H. Inoue, Solidification cracking susceptibility of alloy 718 during additive manufacturing and evaluating method, Journal of Materials

514 Research and Technology 33 (2024) 6389–6396.
515 https://doi.org/10.1016/j.jmrt.2024.11.021.
516 [17] D.G. Eskin, Suyitno, L. Katgerman, Mechanical properties in the semi-solid state and
517 hot tearing of aluminium alloys, Progress in Materials Science 49 (2004) 629–711.
518 https://doi.org/10.1016/S0079-6425(03)00037-9.
519 [18] S. Kou, Solidification and liquation cracking issues in welding, JOM 55 (2003) 37–42.
520 https://doi.org/10.1007/s11837-003-0137-4.
521 [19] P. Kontis, E. Chauvet, Z. Peng, J. He, A. Kwiatkowski da Silva, D. Raabe, C. Tassin, J.-
522 J. Blandin, S. Abed, R. Dendievel, B. Gault, G. Martin, Atomic-scale grain boundary
523 engineering to overcome hot-cracking in additively-manufactured superalloys, Acta
524 Materialia 177 (2019) 209–221. https://doi.org/10.1016/j.actamat.2019.07.041.
525 [20] Q. Han, R. Mertens, M.L. Montero-Sistiaga, S. Yang, R. Setchi, K. Vanmeensel, B. Van
526 Hooreweder, S.L. Evans, H. Fan, Laser powder bed fusion of Hastelloy X: Effects of hot
527 isostatic pressing and the hot cracking mechanism, Materials Science and Engineering:
528 A 732 (2018) 228–239. https://doi.org/10.1016/j.msea.2018.07.008.
529 [21] J.N. Ghoussoub, Y.T. Tang, W.J.B. Dick-Cleland, A.A.N. Németh, Y. Gong, D.G.
530 McCartney, A.C.F. Cocks, R.C. Reed, On the Influence of Alloy Composition on the
531 Additive Manufacturability of Ni-Based Superalloys, Metallurgical and Materials
532 Transactions A 53 (2022) 962–983. https://doi.org/10.1007/s11661-021-06568-z.
533 [22] F.J. Humphreys, Grain and subgrain characterisation by electron backscatter diffraction,
534 Journal of Materials Science 36 (2001) 3833–3854.
535 https://doi.org/10.1023/A:1017973432592.
536 [23] S.I. Wright, M.M. Nowell, D.P. Field, A Review of Strain Analysis Using Electron
537 Backscatter Diffraction, Microscopy and Microanalysis 17 (2011) 316–329.
538 https://doi.org/10.1017/S1431927611000055.

[24] E.M. Lehockey, Y.-P. Lin, O.E. Lepik, Mapping Residual Plastic Strain in Materials Using Electron Backscatter Diffraction, in: A.J. Schwartz, M. Kumar, B.L. Adams (Eds.), Electron Backscatter Diffraction in Materials Science, Springer US, 2000: pp. 247–264. https://doi.org/10.1007/978-1-4757-3205-4_20.

[25] M. Calcagnotto, D. Ponge, E. Demir, D. Raabe, Orientation gradients and geometrically necessary dislocations in ultrafine grained dual-phase steels studied by 2D and 3D EBSD, Materials Science and Engineering: A 527 (2010) 2738–2746. https://doi.org/10.1016/j.msea.2010.01.004.

[26] J.-O. Andersson, T. Helander, L. Höglund, P. Shi, B. Sundman, Thermo-Calc & DICTRA, computational tools for materials science, Calphad 26 (2002) 273–312. https://doi.org/10.1016/S0364-5916(02)00037-8.

[27] B. Sundman, B. Jansson, J.-O. Andersson, The Thermo-Calc databank system, Calphad 9 (1985) 153–190. https://doi.org/10.1016/0364-5916(85)90021-5.

[28] Q. Chen, B. Sundman, Computation of Partial Equilibrium Solidification with Complete Interstitial and Negligible Substitutional Solute Back Diffusion, Materials Transactions 43 (2002) 551–559. https://doi.org/10.2320/matertrans.43.551.

[29] S.A. David, J.M. Vitek, Correlation between solidification parameters and weld microstructures, International Materials Reviews 34 (1989) 213–245. https://doi.org/10.1179/imr.1989.34.1.213.

[30] L. Li, R.W. Messler Jr., The effects of phosphorus and sulfur on susceptibility to weld hot cracking in austenitic stainless steels, Welding Journal 78 (1999) 387s–396s.

[31] S. Singh, J. Andersson, Heat-Affected-Zone Liquation Cracking in Welded Cast Haynes® 282®, Metals 10 (2020) 29. https://doi.org/10.3390/met10010029.

[32] Y. Chen, K. Zhang, J. Huang, S.R.E. Hosseini, Z. Li, Characterization of heat affected zone liquation cracking in laser additive manufacturing of Inconel 718, Materials &

Design 90 (2016) 586–594. https://doi.org/10.1016/j.matdes.2015.10.155.

[33] J. Xu, X. Lin, Y. Zhao, P. Guo, X. Wen, Q. Li, H. Yang, H. Dong, L. Xue, W. Huang, HAZ Liquation Cracking Mechanism of IN-738LC Superalloy Prepared by Laser Solid Forming, Metallurgical and Materials Transactions A 49 (2018) 5118–5136. https://doi.org/10.1007/s11661-018-4826-6.

[34] S. Singh, F. Hanning, J. Andersson, Influence of Hot Isostatic Pressing on the Hot Ductility of Cast Alloy 718: The Effect of Niobium and Minor Elements on the Liquation Mechanism, Metallurgical and Materials Transactions A 51 (2020) 6248–6257. https://doi.org/10.1007/s11661-020-06004-8.

[35] D. Wang, K. Kadoi, K. Shinozaki, M. Yamamoto, Evaluation of Solidification Cracking Susceptibility for Austenitic Stainless Steel during Laser Trans-Varestraint Test Using Two-dimensional Temperature Measurement, ISIJ International 56 (2016) 2022–2028. https://doi.org/10.2355/isijinternational.ISIJINT-2016-302.

[36] T.W. Clyne, G.J. Davies, The influence of composition on solidification cracking susceptibility in binary alloy systems, The British Foundryman 74 (1981) 65–73.

[37] S. Kou, A criterion for cracking during solidification, Acta Materialia 88 (2015) 366–374. https://doi.org/10.1016/j.actamat.2015.01.034.

[38] M. Rappaz, J.-M. Drezet, M. Gremaud, A new hot-tearing criterion, Metallurgical and Materials Transactions A 30 (1999) 449–455. https://doi.org/10.1007/s11661-999-0334-z.

[39] B. Guo, Y. Zhang, Z. Yang, D. Cui, F. He, J. Li, Z. Wang, X. Lin, J. Wang, Cracking mechanism of Hastelloy X superalloy during directed energy deposition additive manufacturing, Additive Manufacturing 55 (2022) 102792. https://doi.org/10.1016/j.addma.2022.102792.

[40] N. Wang, S. Mokadem, M. Rappaz, W. Kurz, Solidification cracking of superalloy

589 single- and bi-crystals, Acta Materialia 52 (2004) 3173–3182.
590 https://doi.org/10.1016/j.actamat.2004.03.047.
591 [41] E. Chauvet, P. Kontis, E.A. Jägle, B. Gault, D. Raabe, C. Tassin, J.-J. Blandin, R.
592 Dendievel, B. Vayre, S. Abed, G. Martin, Hot cracking mechanism affecting a non-
593 weldable Ni-based superalloy produced by selective electron Beam Melting, Acta
594 Materialia 142 (2018) 82–94. https://doi.org/10.1016/j.actamat.2017.09.047.
595 [42] R. Cunningham, C. Zhao, N. Parab, C. Kantzos, J. Pauza, K. Fezzaa, T. Sun, A.D.
596 Rollett, Keyhole threshold and morphology in laser melting revealed by ultrahigh-speed
597 x-ray imaging, Science 363 (2019) 849–852. https://doi.org/10.1126/science.aav4687.
598 [43] M.J. Matthews, G. Guss, S.A. Khairallah, A.M. Rubenchik, P.J. Depond, W.E. King,
599 Denudation of metal powder layers in laser powder bed fusion processes, Acta
600 Materialia 114 (2016) 33–42. https://doi.org/10.1016/j.actamat.2016.05.017.
601 [44] H. Gong, K. Rafi, H. Gu, T. Starr, B. Stucker, Analysis of defect generation in Ti–6Al–
602 4V parts made using powder bed fusion additive manufacturing processes, Additive
603 Manufacturing 1–4 (2014) 87–98. https://doi.org/10.1016/j.addma.2014.08.002.
604 [45] S. Katayama, Defect formation mechanisms and preventive procedures in laser welding,
605 in: S. Katayama (Ed.), Handbook of Laser Welding Technologies, Woodhead
606 Publishing, 2013: pp. 332–373. https://doi.org/10.1533/9780857098771.2.332.
607 [46] J.H. Martin, B.D. Yahata, J.M. Hundley, J.A. Mayer, T.A. Schaedler, T.M. Pollock, 3D
608 printing of high-strength aluminium alloys, Nature 549 (2017) 365–369.
609 https://doi.org/10.1038/nature23894.
610 [47] J.F.S. Markanday, Applications of alloy design to cracking resistance of additively
611 manufactured Ni-based alloys, Materials Science and Technology 38 (2022) 1300–1314.
612 https://doi.org/10.1080/02670836.2022.2068759.
613 [48] X. Xie, F. Zhang, C. Peng, X. Yan, Q. Chao, Y. Li, R. Li, X. Liu, G. Fan, Effect of scan

614 strategy and substrate preheating on crack formation in IN738LC Ni-based superalloy
615 during laser powder bed fusion, Materials Characterization 221 (2025) 114722.
616 https://doi.org/10.1016/j.matchar.2025.114722.
617